



# Design and Analysis of a Snake-Inspired Crawling Robot Driven by Alterable Angle Scales

Donghua Shen, Qi Zhang , Cunjin Wang, Xingsong Wang , and Mengqian Tian

**Abstract**—Inspired by the anisotropic friction of snakes' scales, many snake-like robots actuated by scales have been developed. However, these robots' scales' angle is unalterable, causing them to crawl in only one direction. Moreover, these robots typically require complex controllers to control their locomotion. To address these limitations, the letter proposes a crawling robot with alterable angle scales, a soft actuator, and an autonomous vibrating valve. All scales are strung on a spring wire and can rotate freely, and an airbag can easily control the rotation. The robot can crawl backward after flipping the scales' orientation. A piston located inside the vibrating valve can be periodically pushed by a reset spring and air pressure to achieve reciprocating motion, which results in periodic inflating and deflating of the soft actuator. Such that the crawling robot can move automatically. The locomotion mechanism was analyzed, and a dynamic model was built. The locomotion performance was tested by experiments. The experimental results show that both the forward and backward locomotion speed can be improved by increasing the driving pressure. When the driving pressure is 195 kPa, the robot can crawl forward and backward at the speed of 49.0 mm/s and 38.2 mm/s, respectively.

**Index Terms**—Biomimetics, crawling robot, scale, snake-like robot, soft robot materials and design.

## I. INTRODUCTION

THE abdominal scales of a snake can snag on the rough surface when moving forward, making it much easier to slide forward than backward. The snake's frictional anisotropy with the surface is the primary cause of the ability to crawl forward [1]. The forward driving force is generated by body swing and anisotropic friction [2]. The microscopic and macroscopic structures of snake scales have been studied to reveal the cause of anisotropic friction [3]–[5], it indicates that the friction can be enhanced by the scales' microstructure only on the nanoscale roughness surface. The anisotropic friction at the macro- and microscale is provided by the scales' macroscopic pattern. This

is the reason why snakes have trouble crawling on the smooth surface [6]–[9].

Although this type of motion seems to be less efficient than that of footed animals, snakes' slender and flexible body allows them to move in unstructured terrains, such as narrow caves, debris environment, and pipeline. Inspired by this, many snake-like robots with different driving mechanisms, including wheeled [10], [11], crawler [12], [13], and friction-driven robots [14]–[16], have been developed for detecting small spaces inside some equipment, and search and rescue in ruins. However, most snake-like robots are composed of rigid parts and have low adaptability in complex environments.

Researchers have begun to study snake-like robots actuated by scales for better adaptation in unstructured environments in recent years. Marvi H developed a two-link limbless robot with individually controlled sets of belly scales to improve its crawling ability. The robot uses individual servos to provide spatial and temporal dependence on its belly friction [17]. Wang W developed a scale-driven snake-like robot for climbing rope. The robot can circumvent and jump over obstacles along a cylindrical rope [18]. Ta T D developed a 3D printed scale using two materials with different friction coefficients. This scale allows the snake-like robot to crawl on glass surfaces [19]. Huq N developed a snake-like robot with bellow scales and studied the effects of the scales on movement in different robot parts [20]. Alexander H developed a snake-like robot covered by a 3D printed shell with rigid scales. The robot was driven by motors and can crawl on cobblestone or rough concrete grounds [21]. Inspired by traditional paper-cutting techniques, Ahmad Rafsanjani developed a soft snake-like robot covered by a laser cut snakeskin with many scales. When the robot elongates, its scales can expand and engage with the ground to crawl forward [22].

Furthermore, the anisotropic friction of snakes' scales also inspired the designs of some crawling robots. George M developed an autonomous earthworm-like robot actuated by a bistable valve [23]. Calabrese L developed a scale-driven crawling robot consisting of a planar dielectric elastomer actuator, a beam, and two brushes installed at the root of the beam. The robot can crawl on rough grounds using the brushes' anisotropic friction when it contracts [24]. Ben-Tzvi developed a telescopic crawling robot with cloth skin that can provide anisotropic friction [25]. Paik developed an inchworm robot with three kirigami layers serving as an actuator, a sensor, and a contact pad with directional friction [26]. To better understand anisotropic locomotion, S. P.

Manuscript received September 2, 2020; accepted February 8, 2021. Date of publication February 23, 2021; date of current version March 29, 2021. This letter was recommended for publication by Associate Editor B. Mazzolai and Editor X. Liu upon evaluation of the reviewers' comments. This work was supported by the Scientific Research Foundation of Graduate School of Southeast University (YBPY1850). (Donghua Shen and Qi Zhang are co-first authors.) (Corresponding authors: Xingsong Wang; Mengqian Tian)

The authors are with the School of Mechanical Engineering, Southeast University, Nanjing 211189, China (e-mail: sdh\_engineer@163.com; kichy\_zq@163.com; jiajia1900s@163.com; xswang@seu.edu.cn; tianmq@seu.edu.cn).

This letter has supplementary downloadable material available at <https://doi.org/10.1109/LRA.2021.3061379>, provided by the authors.

Digital Object Identifier 10.1109/LRA.2021.3061379

M. developed a soft sensorized foot module. It can detect the interactions between the foot and the surfaces, which provides a new way to design soft robots for moving on unstructured terrains [27].

As discussed in the above-stated studies, anisotropic friction scales have been used in various snake-like or crawling robots. However, the angle of these robots' scales is unalterable (i.e., they cannot be changed), and the robots are unable to crawl backward. The lack of autonomous backward crawling ability makes it difficult for these robots to withdraw from narrow spaces. Besides, these robots typically require complex controllers to generate movement. Once their controllers are disturbed, the robots may have a high probability of failure in locomotion.

To address these shortcomings, this letter proposes a novel snake-inspired crawling robot that can automatically crawl forward and backward. Unlike the existing crawling robots, the scales' angle can be easily controlled by the airbag, and the backward crawling can be achieved by flipping the scales' orientation. The automatic vibrating valve enables the robot to elongate and contract automatically under the air input with constant pressure. Additionally, the crawling robot can also be assembled in series to produce a long snake-like robot that has high mobility. It can easily crawl out of narrow spaces as each section of the body (i.e., each crawling robot) can crawl actively. Note that no external control but only constant compressed air is used to drive the robot, making the movement stable and simplifying the control system.

## II. STRUCTURAL DESIGN

Fig. 1 shows the design detail of the crawling robot. It is mainly composed of a scale module, a soft actuator, and an autonomous vibrating valve.

### A. Design of the Scale Module

The scales are made of polyethylene terephthalate film (Young's Modulus  $E = 4.33$  GPa, the thickness  $t = 0.3$  mm) using laser cutting. As Fig. 1(A) shows, the main dimensions of the cutting slice are as follows: the length  $h = 8$  mm, the root width  $b_1 = 4$  mm, and the top width  $b_0 = 1.5$  mm. The slices are then bent into scales. The scales have two legs, and each leg has two holes with a diameter of 1.6 mm and 0.8 mm. All scales are strung on the spring wire through the bigger holes, and adjacent scales are attached. These scales can rotate around the axis of the bigger holes. Balls are placed between the legs, and a 0.6 mm diameter rubber band is passed through the small holes and the balls in turn. These balls ensure these scales to be evenly distributed in the spring wire. The two ends of the spring wire are connected to the vibrating valve and the end cover using two connecting rings, as shown in Fig. 1(B).

To flip the scales, an airbag is placed between the valve and the end cover. When compressed air is injected into port B, the airbag inflates and rotates all scales. With the increase of the air pressure, the scales will flip as shown in Fig. 1(C). Once the airbag is deflated, the rubber band will pull the scales' legs and make the scales to return to their initial state.

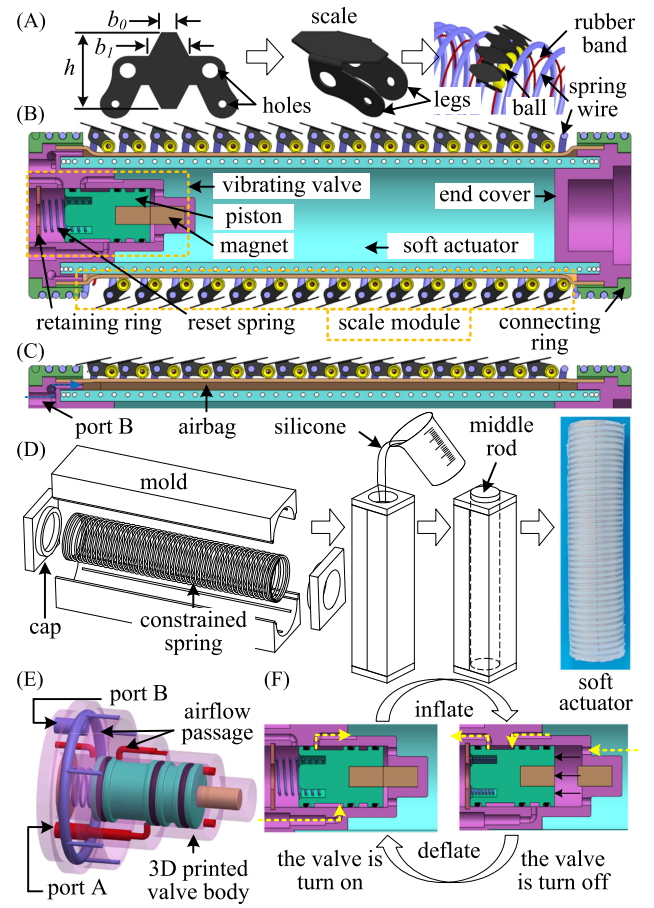


Fig. 1. Design of the crawling robot. (A) structure and assembly process of the scales; (B) the cross-sectional view of the crawling robot. The piston is at the right end of the valve; when air flows into the soft actuator from port A, the soft actuator will inflate and elongate; (C) the airbag is inflated, and the scales' angle is changed; (D) view of the 3D printed mold and fabrication process of the soft actuator; (E) internal flow passage of the vibrating valve. (F) the valve switches between on and off states. When the piston is at the right end, the air flows into the soft actuator from port A, and the soft actuator will inflate and elongate. When the piston is pushed to the left end by the air in the soft actuator, the soft actuator deflates and contracts.

### B. Design and Fabrication of the Soft Actuator

To increase the elongation and constrain the deformation in the radial direction of the actuator upon inflation, a constrained spring is embedded in the soft actuator. The soft actuator is made of Ecoflex0030 silicone, and its fabrication process is shown Fig. 1(D). Firstly, the constrained spring is placed in the 3D printed mold. The silicone is then injected inside the mold. Next, the rod is inserted into the mold and held in place by the caps. Finally, the soft actuator is removed from the mold. On this basis, the soft actuator can elongate along its axis direction when compressed air is injected.

### C. Design of the Vibrating Valve

The valve is mainly composed of a 3D printed valve body, a piston, two magnets, and a reset spring. There are two groups of airflow passage in the valve body (Fig. 1(E)). The passage to

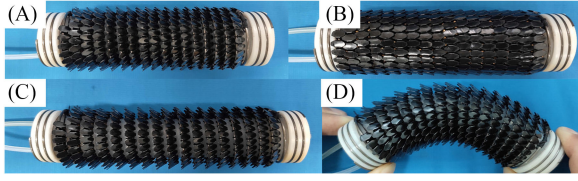


Fig. 2. The prototype of the proposed crawling robot. (A) the crawling robot's original state; (B) changing of the scales' angle; (C) elongation of the crawling robot; (D) bending of the crawling robot.

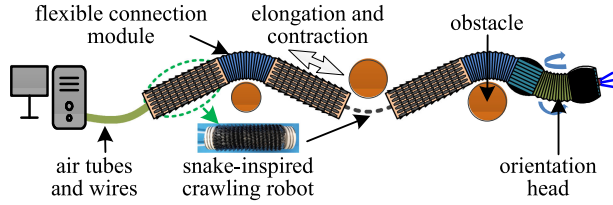


Fig. 3. Overview of a concept snake-like robot system driven by the crawling robots.

port A is used to inflate and deflate the soft actuator cyclically. The passage to port B is used to inflate and deflate the airbag.

The piston is located inside the valve body, and two magnets (4 mm in diameter and 8 mm in length) are fixed to the piston and the valve body, respectively. The magnets can make the piston move faster because the suction drops rapidly when the two magnets separate. A reset spring is installed between the retaining ring and the piston, as shown in Fig. 1(B). In the initial state, the valve is turned on, and the two magnets are attracted together. The crawling robot elongates when compressed air is injected into the soft actuator through port A. Once the soft actuator's air pressure reaches its maximum value ( $P_u$ ), the piston will be pushed against the reset spring's force and magnets' attraction and moved to the left to fit the retaining ring before the valve is turned off. Consequently, the compressed air in the soft actuator is released into the atmosphere, and the crawling robot contracts afterward. When the air pressure in the soft actuator drops to its minimum value ( $P_l$ ), the piston will move to the right until the two magnets are fully attracted, thus beginning a new round. As the piston is pushed by the air pressure in the soft actuator, the soft actuator can periodically elongate and contract. The circulates switch of the valve between on and off is shown in Fig. 1(F).

The prototype of the crawling robot is shown in Fig. 2. It shows that the crawling robot can perform behaviors including elongation, scale reversal, and adaptive bending.

Several crawling robots of the proposed type can also be serially connected using a flexible connection module to form a snake-like robot, as shown in Fig. 3. In the design of the snake-like robot, port A of each crawling robot is connected, as well as that of port B. Therefore, the whole robot only needs two tubes. The tube that connects all ports A controls the independent telescopic motion of each crawling robot. The tube that connects all ports B controls the scales' angle of all crawling robots. Based on this design, the number of tubes used in the snake-like robot

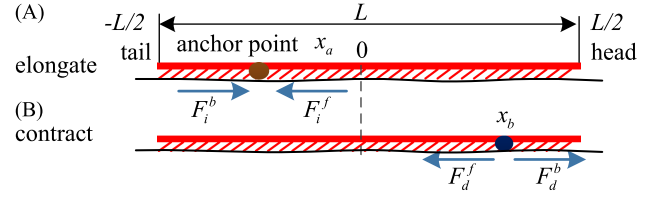


Fig. 4. Analysis of the anchor point. (A) the friction of scales when the crawling robot elongates; (B) the friction of scales when the crawling robot contracts.

is greatly reduced. The robot can bend passively, allowing it to crawl around obstacles under the direction of its head. Note that this letter focuses on the development of this crawling robot.

### III. MODELING

#### A. Analysis of Crawling Properties

To analyze the crawling ability of the crawling robot, this letter conducts the modeling of the scale driving force. The model is based on the following assumptions: (1) when the crawling robot crawls, the scales and the rough surface remain relatively static at a certain point known as the anchor point [22], as shown in Fig. 4; (2) the mass of the crawling robot is evenly distributed; (3) the friction between the robot's body and the rough surface is evenly distributed.

Borrowing the definition of density, the robot's linear density  $\rho$  can be defined as follows:

$$\rho = m/L \quad (1)$$

where  $m$  is the mass of the crawling robot, and  $L$  is the scale module's length.

Fig. 4(A) shows that the frictions on the two sides of the anchor point have opposite directions. The two frictions can be calculated by the following equations:

$$F_i^b = \int_{-L/2}^{x_a} \rho g \mu_b dx \quad (2)$$

$$F_i^f = - \int_{x_a}^{L/2} \rho g \mu_f dx \quad (3)$$

where  $x_a$  is the anchor point when the crawling robot elongates,  $F_i^b$  and  $F_i^f$  are the frictions on the two sides of the anchor point,  $\mu_b$  and  $\mu_f$  are the backward and forward friction coefficients.

According to the force balance theorem, we have:

$$\sum F = F_i^b + F_i^f = 0 \quad (4)$$

Substituting (2) and (3) into (4) produces the following:

$$\frac{x_a}{L} = -\frac{1}{2} \left( \frac{\mu_b - \mu_f}{\mu_b + \mu_f} \right) = -\frac{1}{2} C_f \quad (5)$$

where  $C_f$  is the anchoring coefficient,  $C_f = \frac{\mu_b - \mu_f}{\mu_b + \mu_f}$ .

In the same way, the friction of the scales when the crawling robot contracts (Fig. 4(B)) can be described with the following



equations:

$$F_d^b = \int_{x_b}^{\frac{L}{2}} \rho g \mu_b dx \quad (6)$$

$$F_d^f = - \int_{-\frac{L}{2}}^{x_b} \rho g \mu_f dx \quad (7)$$

$$\sum F = F_d^b + F_d^f = 0 \quad (8)$$

where  $x_b$  is the anchor point when the crawling robot contracts.  $F_d^b$  and  $F_d^f$  are the frictions on both sides of the anchor point.

Substituting (6) and (7) into (8), we have:

$$\frac{x_b}{L} = \frac{1}{2} \left( \frac{\mu_b - \mu_f}{\mu_b + \mu_f} \right) = \frac{1}{2} C_f \quad (9)$$

It can be seen from (5) and (9) that the larger  $\mu_b/\mu_f$  is, the closer the anchor point will be to both sides of the crawling robot, and the higher the crawling ability of the robot. If  $\mu_b/\mu_f \rightarrow 1$ , the anchor point is close to the middle of the crawling robot. Under this circumstance, the middle position of the crawling robot is anchored to the ground, and the parts on both sides of the anchor point make equal amplitude telescopic movements. In this case, the crawling robot cannot generate an effective crawling driving force and may have low mobility.

Note that when the scales' structure parameters are changed, both the  $\mu_b$  and  $\mu_f$  will change. However, after  $\mu_b$  and  $\mu_f$  are measured through experiments, the position of the anchor point can still be calculated through (5) and (9).

### B. Inflation and Deflation Process of the Soft Actuator

As Fig. 1(F) shows, the vibrating valve has two alternate states (on and off). To simplify the analysis, the piston's motion process is ignored. The maximum and minimum pressure ( $P_u$  and  $P_l$ ) in the soft actuator are calculated according to the static force on the piston in the two states.

According to the force balance of the piston,  $P_u$  can be determined by (10) in the inflation process, and  $P_l$  can be determined by (11) in the deflation process. Note that as the two magnets are separated in the deflation process, the magnet's attraction on the piston is ignored.

$$P_u S_0 - F_c - k_1 x_0 - F_{fr} = 0 \quad (10)$$

$$k_1 (x_0 + \delta) - P_l S_0 - F_{fr} = 0 \quad (11)$$

where  $S_0$  is the area of the piston,  $F_c$  is the magnets' attraction,  $k_1$  is the stiffness of the reset spring,  $x_0$  is the pre-compression of the reset spring,  $F_{fr}$  is the maximum static friction of the piston, and  $\delta$  is the maximum stroke of the piston.

Inspired by the analytical method of pneumatic systems, we use the Sanville flow equation [28] to analyze the soft actuator's inflation and deflation process, as (12) shows.

$$q_m = \begin{cases} C_d \frac{A_1 p_i}{\sqrt{T}} \sqrt{\frac{2K}{R(K-1)}} \sqrt{\left(\frac{p_o}{p_i}\right)^{\frac{2}{K}} - \left(\frac{p_o}{p_i}\right)^{\frac{K+1}{K}}}, & \frac{p_o}{p_i} > C_P \\ C_d \frac{A_1 p_i}{\sqrt{T}} \sqrt{\frac{K}{R} \left(\frac{2}{K+1}\right)^{\frac{K+1}{K}}}, & \frac{p_o}{p_i} \leq C_P \end{cases} \quad (12)$$

where  $C_d$  is the flow coefficient,  $A_1$  is the port area of the vibrating valve,  $K$  is the specific heat ratio,  $p_i$  and  $p_o$  are the input and output pressures of the vibrating valve, respectively, and  $C_P$  is the critical pressure ratio.

Whenever the vibrating valve is turned on and off,  $p_i$  and  $p_o$  will change accordingly. When the vibrating valve is turned on,  $p_i$  and  $p_o$  can be expressed as:

$$\left. \begin{aligned} p_i &= P_s \\ p_o &= p \end{aligned} \right\} \quad (13)$$

where  $P_s$  and  $p$  are the driving pressure (input air pressure of port A) and the pressure in the soft actuator, respectively.

When the vibrating valve is turned off, the two pressures are:

$$\left. \begin{aligned} p_i &= p \\ p_o &= p_e \end{aligned} \right\} \quad (14)$$

where  $p_e$  is the atmospheric pressure.

According to the continuity equation, we have:

$$q_m = \frac{dm_a}{dt} \quad (15)$$

According to the ideal gas law, we can get:

$$pV = m_a RT \quad (16)$$

where  $R$  is the ideal gas constant,  $m_a$  is the gas mass,  $T$  is the gas temperature,  $p$  is the gas pressure, and  $V$  is the gas volume.

Taking the derivation of both sides of (16), we can obtain the following:

$$\frac{d(pV)}{dt} = \frac{dp}{dt} V + \frac{dV}{dt} p = RT \frac{dm_a}{dt} \quad (17)$$

The volume of the inner cavity of the soft actuator can be described as follows:

$$V = A_0 (l_0 + x) \quad (18)$$

where  $A_0$  is the cross-sectional area of the inner cavity,  $l_0$  is the original length of the cavity, and  $x$  is the elongation of the soft actuator.

Substituting (18) into (17), we obtain the following:

$$A_0 (l_0 + x) \dot{p} + A_0 \dot{x} p = RT q_m \quad (19)$$

If one end of the crawling robot is fixed, the crawling robot can be forced to vibrate under air pressure. The kinetic equation of the crawling robot can be obtained:

$$0.5m\ddot{x} + c\dot{x} + F(x) - (p - p_e) A_0 = 0 \quad (20)$$

where  $F(x)$  is the elastic force equation of the soft actuator, and it can be obtained through experiments.

The crawling speed  $v$  and the crawling displacement  $s$  can be calculated as follows:

$$v = \begin{cases} -0.5(1 - C_f) \dot{x}, & \dot{x} \geq 0 \\ -0.5(1 + C_f) \dot{x}, & \dot{x} < 0 \end{cases} \quad (21)$$

$$s = \int_0^t v dt \quad (22)$$

The soft actuator's dynamic air pressure during inflation and deflation processes can be calculated using (12). The crawling

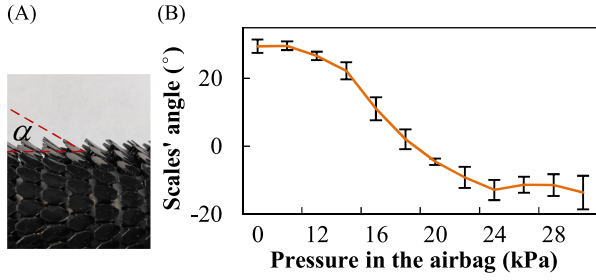


Fig. 5. The scales' angle when the airbag is inflated at different air pressures. (A) photograph of the crawling robot's scales; (B) evolution of scales' angle ( $\alpha$ ) as a function of air pressure. Each angle is measured five times, and the error bar is the standard deviation of the five measurements.

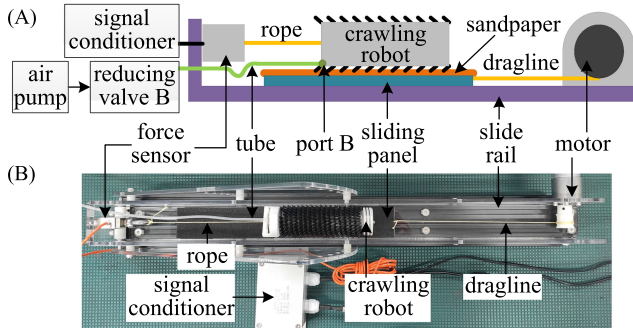


Fig. 6. Friction measurement setup. (A) schematic of the experimental setup; (B) experimental platform for measuring the friction coefficient between the crawling robot and the rough surface.

robot's dynamic displacement and velocity of telescopic motion can be calculated by substituting the results of (12) into (20). By substituting the above results into (21) and (22) and computing with the anchoring coefficient, the crawling robot's dynamic crawling speed and displacement can be calculated. Therefore, the crawling robot's crawling characteristics can be predicted by the above modeling analysis.

#### IV. SIMULATION AND EXPERIMENT

##### A. Scale Friction Characteristic Experiment

To verify the ability to change the scales' angle, the angle variation is tested under different air pressures. In this experiment, the crawling robot is photographed when the airbag is inflated at different air pressures, as shown in Fig. 5(A). The scales' angle is measured using the photograph obtained above. Experimental results are shown in Fig. 5(B). It shows that the scales' angle gradually decreases as the air pressure in the airbag increases. The scales will flip to the reverse direction when the scales' angle decreases to zero. The reverse turning angle of the scales reaches its limit and stabilizes at  $-12^\circ$  when the airbag's air pressure exceeds 24 kPa.

On this basis, the friction between the crawling robot and a rough surface is tested. The schematic of the experimental setup is shown in Fig. 6(A). In the experiment, 80-mesh sandpaper is used as a rough surface, and it is stuck to a sliding panel. A motor drags the sliding panel to move at a constant speed, and

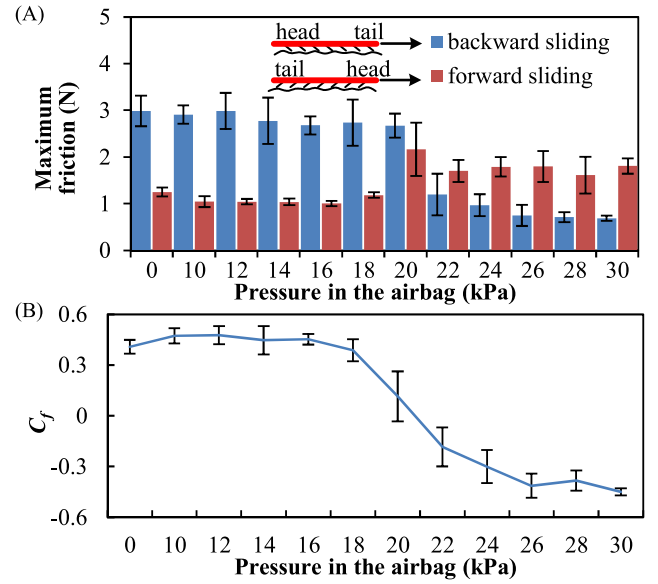


Fig. 7. Experimental results of the friction between the crawling robot and the rough surface. (A) the maximum static friction of the crawling robot under different airbag's air pressures; (B) the anchoring coefficient; Each experiment is repeated five times, and the error bar in the figure is the standard deviation of each experimental data.

the crawling robot is placed on the panel. The crawling robot is connected to a force sensor (DYM-H103) to measure the friction in backward and forward sliding. An air pump is connected to a reducing valve B and then connected to port B. By adjusting the reducing valve's output pressure, pressures in the airbag can be adjusted accordingly. The platform is shown in Fig. 6(B).

Fig. 7(A) shows the friction between the crawling robot and the rough surface when the airbag is inflated at different air pressures. The anchoring coefficient  $C_f$  can be calculated using the backward and forward sliding friction, and the results are shown in Fig. 7(B). It can be observed from the results that the crawling robot has an optimal anchoring coefficient at a pressure of 12 kPa. At this pressure, the angle of the scales is  $26.7^\circ$ . In this state, the crawling robot can crawl forward more efficiently. When the pressure exceeds 22 kPa, all scales reverse and the crawling robot crawls backward. The anchoring coefficient of the reverse crawl can be improved by further increasing the pressure. The anchoring coefficient cannot be further improved once the pressure exceeds 26 kPa. Therefore, the airbag's air pressures are set at 12 kPa and 26 kPa to obtain the better crawling capability in the following dynamic crawling experiments.

##### B. Elastic Force Characteristic of the Soft Actuator

In this experiment, the soft actuator is inflated at different air pressures. The elongation of the soft actuator is measured. The soft actuator's elastic force can be calculated from (23) in equilibrium.

$$F_t = p_a A_0 \quad (23)$$

where  $p_a$  is the pressure in the soft actuator.

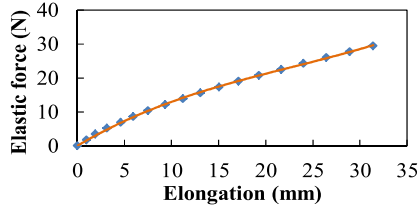


Fig. 8. Elastic force characteristic of the soft actuator.

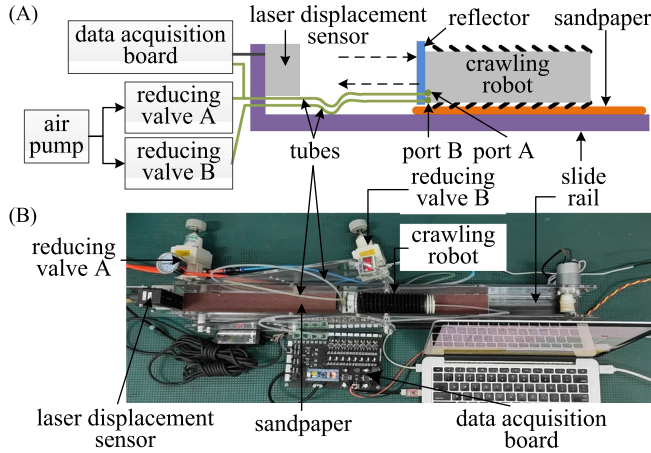


Fig. 9. The platform for the crawling robot crawling experiment. (A) schematic of the experimental setup; (B) experimental platform.

Experimental results are shown in scattered points in Fig. 8. It can be seen that the soft actuator's elastic force is nonlinear. To obtain a continuous elastic force equation, a cubic polynomial is used to fit the experimental data, as shown in (24). It can be used for the simulation analysis of the established theoretical model.

$$F(x) = 0.0006x^3 - 0.0416x^2 + 1.6518x \quad (24)$$

### C. Dynamic Crawling Experiment

To verify the theoretical model and test the crawling characteristics, we measured the dynamic air pressure in the soft actuator and the robot's crawling displacement using our experimental platform. The schematic of the experimental setup is shown in Fig. 9(A). In the experiment, 80-mesh sandpaper is stuck to the slide rail and used as a rough surface. The crawling robot is placed on the sandpaper and can crawl freely on it. A reflector is fixed on the crawling robot's tail, such that the laser displacement sensor (Keyence IL-300) can measure the crawling displacement of the robot. The soft actuator's air pressure is measured through a tube by a pressure sensor on the data acquisition board. An air pump is connected to the air inlets of the reducing valve A and B, then connected to ports A and B separately. By adjusting the reducing valves' output pressure, pressures in the crawling robot and the airbag can be adjusted accordingly. The experimental platform is shown in Fig. 9(B). The main structural parameters of the crawling robot used are shown in Table I.

Fig. 10(A) shows the simulation and experimental results of the soft actuator's dynamic air pressure. It illustrates the

TABLE I  
THE MAIN STRUCTURAL PARAMETERS OF THE CRAWLING ROBOT

Parameter	Value
$l_0$	100mm
$d_0$	1mm
$A_0$	283.5mm <sup>2</sup>
$d$	113mm
$m$	148g

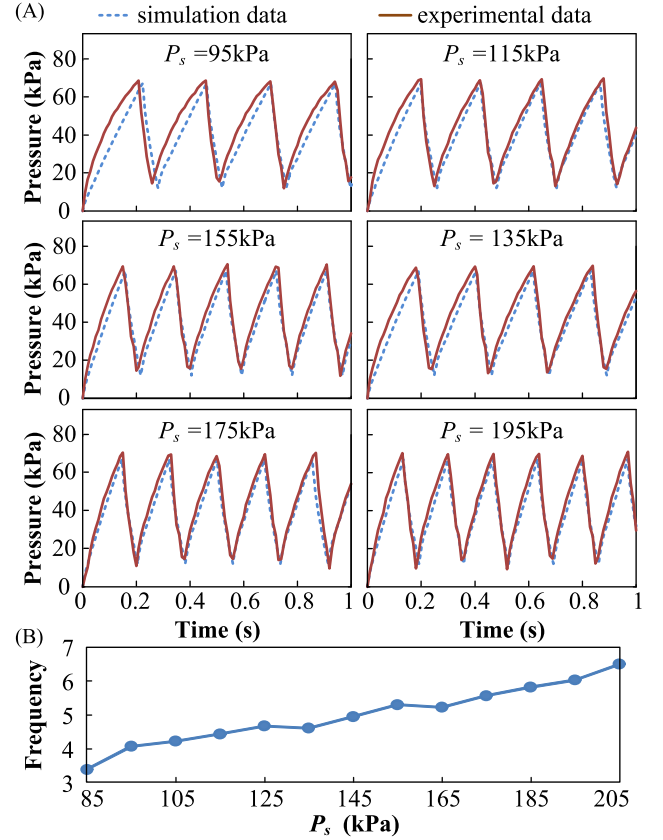


Fig. 10. Periodic vibration of the crawling robot. (A) the soft actuator's dynamic pressure under different driving pressures; (B) the relationship between the vibration frequency of the crawling robot and the driving pressures.

periodic inflation and deflation of the soft actuator. The peak and lowest values of the dynamic air pressure ( $P_u$  and  $P_l$ ) in the soft actuator are the same when different driving pressure is applied. This is because  $P_u$  and  $P_l$  are only affected by the magnets' attraction, the reset spring's force, and the piston's friction. As the driving pressure increases, the crawling robot's vibration frequency increases gradually, as shown in Fig. 10(B). Experimental results and simulation results are consistent, indicating that the mathematical model can effectively describe the crawling robot's autonomous vibration characteristics.

The forward and backward crawling processes of the crawling robot in the platform are shown in Fig. 11. The dynamic crawling displacement and average crawling speed in the experiment are shown in Fig. 12. It can be seen that the crawling robot exhibits intermittent crawling characteristics. The experimental results are consistent with the simulation results. Therefore,



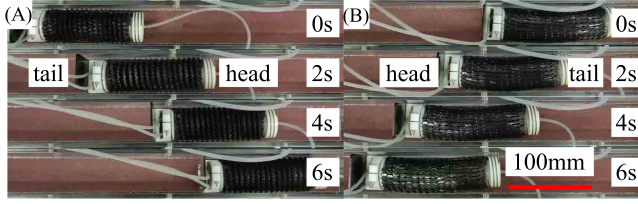


Fig. 11. Crawling robot's crawling process. (A) forward crawling of the crawling robot; (B) backward crawling of the crawling robot. In this experiment, the airbag's air pressures are set at 12 kPa and 26 kPa for forward and backward crawling, respectively.

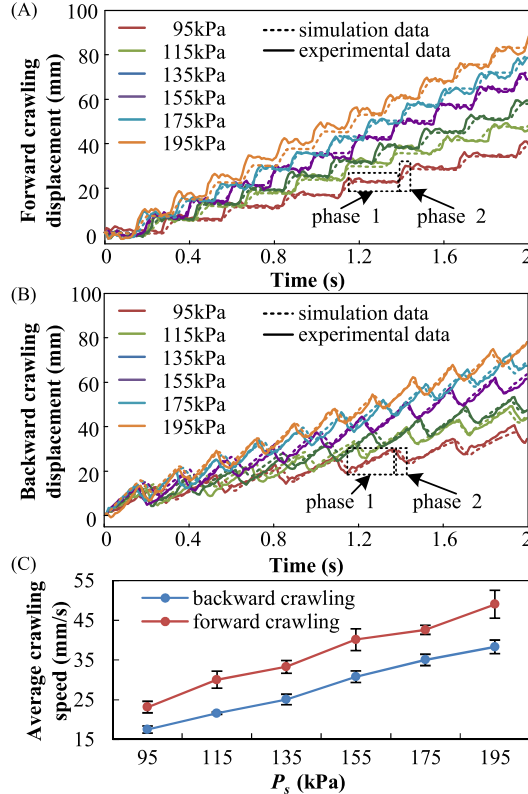


Fig. 12. The experimental and simulation results of the crawling robot's dynamic crawling displacement and average crawling speed. (A) and (B) show the dynamic forward and backward crawling displacements; (C) shows the average forward and backward crawling speeds.

the crawling robot's crawling characteristics can be predicted through simulation.

Following the forward and backward crawling displacements shown in Fig. 12 (A) and (B), it can be seen that the crawling robot has a forward phase and a backward phase in its crawling cycle. The forward and backward phase is caused by the crawling robot's periodic telescopic crawling. The displacement of the crawling robots' tail is measured during forward crawling. The crawling robot's anchor point is close to the tail when the crawling robot elongates. In this case, the crawling robot extends forward while the tail remains still (phase 1 in Fig. 12(A)). When the crawling robot contracts, the anchor point moves close to the head of the crawling robot, the tail moves forward, while the head

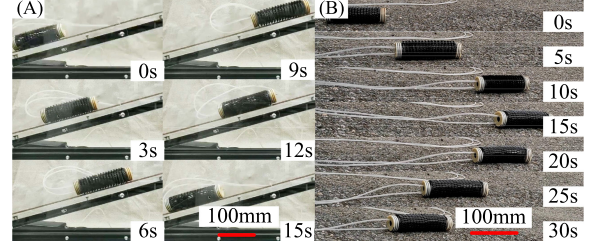


Fig. 13. Crawling ability verification. (A) crawling robot climbs a ramp covered by 80-mesh sandpaper; (B) crawling robot moves on asphalt. In the two experiments, the driving pressure is set at 155 kPa.

remains still (phase 2 in Fig. 12(A)). The regularity of backward crawling is similar to that of forward crawling. The difference is that the tail becomes the head, and the displacement of the head is measured when it is crawling backward. In phase 1 of Fig. 12(B), the crawling robot elongates. In phase 2 of Fig. 12(B), the crawling robot contracts. During backward crawling, the anchoring coefficient is slightly smaller, which causes the anchor point to be closer to the middle of the crawling robot and leads to a longer reverse distance in phase 2 of each crawling cycle, reducing the crawling robot's average crawling speed.

The crawling robot's average forward and backward crawling speeds under different driving pressures are shown in Fig. 12(C). It can be seen that the crawling robot's speed increases as the driving pressure increases, and both the crawling speed and driving pressure have a relatively linear relationship. The crawling robot's forward and backward crawling speeds are 49.0 mm/s and 38.2 mm/s, respectively, when the driving pressure is 195 kPa.

Climbing a ramp and crawling in a real-world scenario are evaluated to further verify the crawling robot's crawling ability, as shown in Fig. 13(A) and (B). In the climbing ramp experiment, the 80-mesh sandpaper is pasted on a ramp. Experimental results show that the crawling robot can easily climb over a 15° ramp. When climbing uphill, the crawling robot crawls forward. The uphill crawling speed is 25.4 mm/s, which is slower than crawling on a rough horizontal surface. It may be the gravity of the crawling robot that hinders its speed.

In the experiment of crawling on asphalt, the crawling robot can crawl both in forward and backward directions. The average forward and backward crawling speeds are 33.7 mm/s and 18.8 mm/s, respectively. It is slower than crawling on the experimental platform due to asphalt is less uniform than sandpaper. During crawling, part of the crawling robot is detached from the asphalt ground, making the crawling robot to elongate and contract in situ and not crawl forward. Moreover, there is no side obstacle on the ground to restrain crawling direction, and it is easy for the crawling robot to crawl sideways. However, this problem can be easily solved in the snake-like robot in which the robot's orientation head can guide the direction of the crawling robot.

## V. CONCLUSION

This letter presents a novel snake-inspired crawling robot with alterable angle scales and an autonomous vibrating valve.

The airbag can easily control the scales' angle, and backward crawling is achieved by flipping the scales' orientation. By inputting constant-pressure air into the vibrating valve, the valve can inflate and deflate the soft actuator periodically, causing the soft actuator to elongate and contract regularly. Thus, the crawling robot can crawl automatically without any controller, which significantly enhances the crawling robot's movement's reliability.

A theoretical model was developed to predict the crawling characteristics of the crawling robot. An experimental platform was built to assess the crawling characteristics and validate the rationality of the model. In the experiment, 80-mesh sandpaper was used to simulate a rough surface. The simulation and experimental results are consistent when compared. The experimental results show that the crawling robot can effectively crawl on the rough surface and move backward when the scales flip. The crawling speed can be significantly increased by increasing the driving pressure. Furthermore, two more experiments were performed to test the crawling robot's mobility; it is validated that the crawling robot can successfully climb on both ramp and asphalt.

In future work, we will build a slender snake-like robot by connecting several crawling robots and will carry out more complex experiments on the snake-like robot's locomotion ability. The entire long snake-like robot has high mobility because each crawling robot can actively crawl. The ability to crawl backward can effectively prevent the snake-like robot from getting stuck in a narrow environment.

## REFERENCES

- [1] D. L. Hu, J. Nirody, T. Scott, and M. J. Shelley, "The mechanics of slithering locomotion," in *Proc. Natl. Acad. Sci.*, vol. 106, no. 25, pp. 10 081–10 085, Apr. 2009.
- [2] H. Marvi, J. P. Cook, J. L. Streater, and D. L. Hu, "Snakes move their scales to increase friction," *Biotribol.*, vol. 5, pp. 52–60, Nov. 2016.
- [3] M. J. Benz, A. E. Kovalev, and S. N. Gorb, "Anisotropic frictional properties in snakes," in *Proc. SPIE Int. Soc. Opt. Eng.*, Mar. 2012, Art. no. 83390X, doi: [10.1117/12.916972](https://doi.org/10.1117/12.916972).
- [4] A. H. Abdel-Aal, "Surface structure and tribology of legless squamate reptiles," *J. Mech. Behav. Biomed. Mater.*, vol. 79, pp. 354–398, Mar. 2018.
- [5] L. Zheng *et al.*, "Coupling effect of morphology and mechanical properties contributes to the tribological behaviors of snake scales," *J. Bionic Eng.*, vol. 15, no. 3, pp. 481–493, May 2018.
- [6] A. E. Filippov and S. N. Gorb, "Modelling of the frictional behaviour of the snake skin covered by anisotropic surface nanostructures," *Sci. Rep.*, vol. 6, no. 1, Mar. 2016, Art. no. 23539.
- [7] M. J. Baum, A. E. Kovalev, J. Michels, and S. N. Gorb, "Anisotropic friction of the ventral scales in the snake *lampropeltis getula californica*," *Tribol. Lett.*, vol. 54, no. 2, pp. 139–150, May 2014.
- [8] C. Greiner and M. Schafer, "Bio-inspired scale-like surface textures and their tribological properties," *Bioinspir. Biomim.*, vol. 10, no. 4, May 2015, Art. no. 44001.
- [9] R. A. Berthé, G. Westhoff, H. Bleckmann, and S. N. Gorb, "Surface structure and frictional properties of the skin of the amazon tree boa *corallus hortulanus* (squamata, boidae)," *J. Comp. Physiol.*, vol. 195, no. 3, pp. 311–318, Mar. 2009.
- [10] M. Tanaka, M. Nakajima, Y. Suzuki, and K. Tanaka, "Development and control of articulated mobile robot for climbing steep stairs," *IEEE-ASME Trans. Mechatron.*, vol. 23, no. 2, pp. 531–541, Apr. 2018.
- [11] K. Ito and H. Maruyama, "Semi-autonomous serially connected multi-crawler robot for search and rescue," *Adv. Robot.*, vol. 30, no. 7, pp. 489–503, Apr. 2016.
- [12] M. Neumann, T. Predki, L. Heckes, and P. Labenda, "Snake-like, tracked, mobile robot with active flippers for urban search-and-rescue tasks," *Ind. Robot.*, vol. 40, no. 3, pp. 246–250, Nov. 2013.
- [13] K. Ito and R. Murai, "Snake-like robot for rescue operations - proposal of a simple adaptive mechanism designed for ease of use," *Adv. Robot.*, vol. 22, no. 6, pp. 771–785, 2008.
- [14] P. Liljebäck, K. Y. Pettersen, O. Stavdahl, and J. T. Gravdahl, "Snake robot locomotion in environments with obstacles," *IEEE-ASME Trans. Mechatron.*, vol. 17, no. 6, pp. 1158–1169, Dec. 2012.
- [15] C. Wright, A. Buchan, B. Brown, J. Geist, and M. Schwerin, and Howie, "Design and architecture of the unified modular snake robot," in *Proc. IEEE Int. Conf. Rob. Autom.*, May 2012, pp. 4347–4354.
- [16] F. Trebuña, I. Virgala, M. Pástor, T. Lipták, and L. Miková, "An inspection of pipe by snake robot," *Int. J. Adv. Robot. Syst.*, vol. 13, no. 5, pp. 1–12, Oct. 2016.
- [17] H. Marvi, G. Meyers, G. Russell, and D. L. Hu, "Scalybot: A. snake-inspired robot with active control of friction," in *ASME Dyn. Syst. Control Conf. Bath/ASME Symp. Fluid Power Motion Control*, Nov. 2011, pp. 443–450.
- [18] W. Wang, Z. Yang, L. Guo, G. Wu, Y. Bai, and S. Li, "Gait planning of a scale-driven snake-like robot for winding and obstacle crossing," *Adv. Mech. Eng.*, vol. 9, no. 11, Nov. 2017, Art. no. 1687814017731038, doi: [10.1177/1687814017731038](https://doi.org/10.1177/1687814017731038).
- [19] T. D. Ta, T. Umedachi, and Y. Kawahara, "Design of frictional 2D-anisotropy surface for wriggle locomotion of printable soft-bodied robots," in *Proc. IEEE Int. Conf. Rob. Autom.*, May 2018, pp. 6779–6785.
- [20] N. Huq, M. Khan, A. Shafie, M. Billah, and S. Ahmmad, "Motion investigation of a snake robot with different scale geometry and coefficient of friction," *Robot.*, vol. 7, no. 2, Jun. 2018, Art. no. 18, doi: [10.3390/robotics7020018](https://doi.org/10.3390/robotics7020018).
- [21] A. H. Chango and P. A. Vela, "Evaluation of bio-inspired scales on locomotion performance of snake-like robots," *Robot.*, vol. 37, no. 8, pp. 1–18, Aug. 2019.
- [22] A. Rafsanjani, Y. Zhang, B. Liu, S. M. Rubinstein, and K. Bertoldi, "Kirigami skins make a simple soft actuator crawl," *Sci. Robot.*, vol. 3, no. 15, Feb. 2018, Paper eaar7555.
- [23] P. Rothemund *et al.*, "A soft, bistable valve for autonomous control of soft actuators," *Sci. Robot.*, vol. 3, no. 16, Mar. 2018, Paper eaar7986.
- [24] L. Calabrese, A. Berardo, D. D. Rossi, M. Gei, and G. Fantoni, "A soft robot structure with limbless resonant, stick and slip locomotion," *Smart Mater. Struct.*, vol. 28, no. 10, Oct. 2019, Art. no. 104005.
- [25] Wael, Saab, Peter, Racioppo, Anil, P. Kumar, and Ben-Tzvi, "Design of a miniature modular inchworm robot with an anisotropic friction skin," *Robotica*, vol. 37, no. 3, pp. 521–538, Mar. 2019.
- [26] A. Firouzeh, T. Higashisaka, K. Nagato, K. J. Cho, and J. Paik, "Stretchable kirigami components for composite meso-scale robots," *IEEE Robot. Autom. Lett.*, vol. 5, no. 2, pp. 1883–1890, Apr. 2020.
- [27] S. P. M. Babu, F. Visentin, A. Sadeghi, A. Mondini, and B. Mazzolai, "A soft sensorized foot module to understand anisotropic terrains during soft robot locomotion," *IEEE Robot. Autom. Lett.*, vol. 5, no. 3, pp. 4055–4061, Apr. 2020.
- [28] S. Xie, J. Mei, H. Liu, and P. Wang, "Motion control of pneumatic muscle actuator using fast switching valve," in *Lect. Notes Electr. Eng.*, Guangzhou, Dec. 2016, pp. 1439–1451.